Investigating electromagnetically-induced transparency spectral lineshape distortion due to non-uniform fields in Rydberg atom electrometry[a)]

Andrew P. Rotunno,[1] Christopher L. Holloway,[1, b)] Nikunjkumar Prajapati,[1] Samuel Berweger,[1] Alexandra B. Artusio-Glimpse,[1] Roger Brown,[1] Matthew Simons,[1] Amy K. Robinson,[2] Baran N. Kayim,[3] Michael A. Viray,[3] Jasmine F. Jones,[3] Brian C. Sawyer,[3] Robert Wyllie,[3] Thad Walker,[4] Richard W. Ziolkowski,[5] Steven R. Jefferts,[6] Steven Geibel,[6] Jonathan Wheeler,[6] and Eric Imhof[6]

[1)]*National Institute of Standards and Technology, Boulder, CO 80305, USA*
[2)]*ANSYS, Inc, Boulder, CO 80301, USA*
[3)]*Georgia Tech Research Institute, Atlanta, GA, 30332, USA*
[4)]*Department of Physics, University of Madison-Wisconsin, Madison, WI, 53706, USA*
[5)]*University of Arizona, Tucson, AZ 85721, USA*
[6)]*Northrop Grumman, Woodland Hills, CA, 91361, USA*

(Dated: 25 August 2023)

We investigate the effects of spatially non-uniform radio-frequency electric (E) field amplitudes on the spectral lineshapes of electromagnetically induced transparency (EIT) signals in Rydberg atomic systems used in electrometry (i.e., the metrology of E-field strengths). Spatially non-uniform fields distort the EIT spectra from that of an ideal case, and understanding this distortion is important in the development of Rydberg atom-based sensors, as these distortions can limit accuracy and sensitivity. To characterize this distortion, we present a model that approximates the atom vapor as a multi-layered media and then uses Beer's law to combine the absorption through its many discrete thin segments. We present a set of expected line distortions caused by various RF electric-field distributions found in practice. This provides an intuitive diagnostic tool for experiments. We compare this model to measured experimental atomic spectra in both two-photon and three-photon excitation schemes in the presence of non-uniform radio-frequency fields. We show that we can accurately model and reproduce the EIT lineshape distortion observed in these experimental data.

I. INTRODUCTION

In recent years, Rydberg atom spectroscopy has been a fruitful method for making traceable measurements of radio-frequency (RF) electric (E) field amplitudes[1]. In these sensors, Rydberg atom energies are observed via electromagnetically induced transparency (EIT). With on-resonance RF fields, spectral lines can be split with applied resonant electric fields via the Autler-Townes (AT) effect, and with off-resonance ones, lines are shifted in energy by ac Stark effects. By measuring these effects carefully, RF field amplitude[2–8] can be measured traceable to the International System of Units (SI)[9], as well as polarization[10,11], and phase[12,13] of an RF field, yielding numerous applications[1].

Because of their large dipole moments, Rydberg atoms respond sensitively to an incident RF E-field. The typical method in Rydberg-atom electrometry is to utilize EIT/AT schemes to read out the response of the atoms. There are various EIT schemes that have been used. In this paper we experimentally and theoretically study spatially inhomogeneous RF field sensing to comprehensively understand the RF field variations that frequently occur in experimental efforts. We examine both the two-optical photon and three-optical photon schemes shown in Fig. 1, where (a) corresponds to a cesium ^{133}Cs system, and (b) corresponds to a rubidium ^{87}Rb system.

An example of an experimental EIT signal when no RF E-field is applied as a function of coupling laser detuning (Δ_c) is illustrated in Fig. 2 (black trace with peak at $\Delta_c = 0$). This

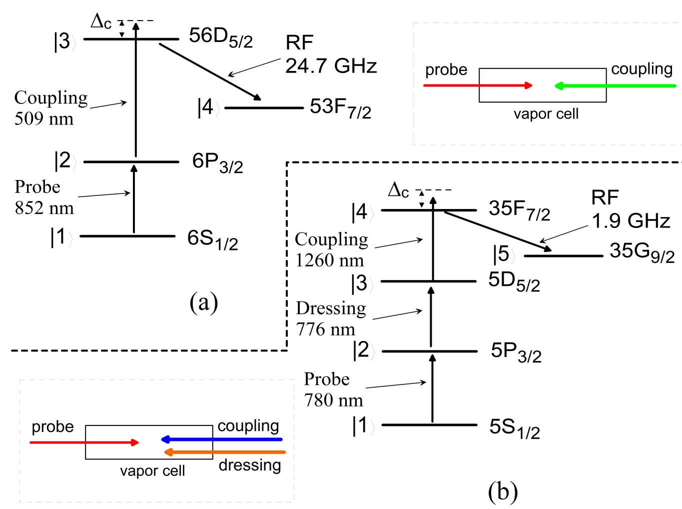

FIG. 1. EIT schemes (a) two-photon ^{133}Cs excitation scheme, and (b) three-photon ^{87}Rb excitation scheme. We use co-linear laser propagation arrangements in both these systems.

experimental data is for the three-photon scheme shown in Fig. 1(b) and details on this experiment are given in Sec. IV. When an on-resonant RF field is applied, AT splitting of the EIT signal occurs, see Fig. 2 (green trace with well defined peaks at $\Delta_c/2\pi \approx \pm 160$ MHz). In these types of measurements, the atom interaction region (i.e., the region where the RF field is measured) is typically a long cylinder for the case of counter-propagating EIT schemes, where the cylinder has a diameter that is the laser beam size, and the length is the region where the beam encounters the atomic vapor. The data

[a)]Publication of the U.S. government, not subject to U.S. copyright.
[b)]christopher.holloway@nist.gov

shown in Fig. 2 (labeled "Uniform field") corresponds to the case when the RF field is uniform across the laser beam propagation path (the atom interaction region); and as such, we see symmetric Gaussian/Lorentzian lineshapes. When the RF field is non-uniform across the atom-interaction region, the EIT spectra becomes distorted. Fig. 2 (the trace labeled as "Standing wave") shows the spectra for a RF standing wave across the laser propagation path (i.e., a non-uniform E-field across the atom interaction region). This standing wave distribution is a result of how the RF is applied, see Sec. IV. For the non-uniform field case the spectrum is distorted, i.e., it is broadened with additional peaks. These non-ideal lineshapes affect the ability to make accurate E-field measurements. In fact, RF tuners (i.e., matching devices) have been used to remove standing wave effects in waveguides for the purpose of improving and/or correcting the lineshape distortion of EIT signals for accurate RF power measurements in Rydberg sensors[14].

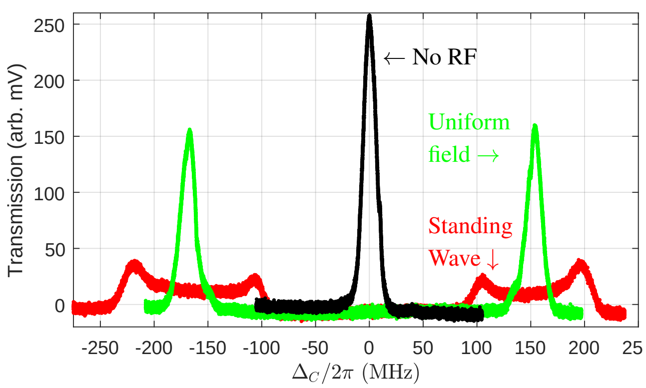

FIG. 2. Measured EIT spectra for the three-photon scheme shown in Fig. 1(b). We compare three cases: No RF field, the uniform applied field or 'uniform field' case, and an anti-optimized case with a significant standing wave non-uniformity present.

The sensitivity and accuracy of an E-field measurement is directly related to the ability to precisely determine the AT splitting[9] or the beat-note strength when a local oscillator is used in a Rydberg mixer scheme[8]. For example, the difficulty in determining the AT peak location is part of the uncertainty budget in E-field measurements[15]. The standing-wave result (red trace in Fig. 2) clearly indicates the difficulty in determining the AT splitting of an E-field measurement when compared to the uniform field case (green trace in Fig. 2). In particular, the applied E-field strength cannot be determined accurately with AT splitting when the two-peak structure is present as the RF standing wave case illustrates.

A major thrust in Rydberg atom electrometry is the development of deployable sensors with fundamental limits on accuracy and sensitivity for applications such as metrology-grade measurements and for atom-based receivers. To achieve this, it is imperative to understand the sources of distortion of the EIT lineshape under different operational conditions. While atomic spectra distortions can be caused from various sources, in this paper we focus on the effects from non-uniform fields.

The non-uniformity in the E-field can manifest from several sources, ranging from the RF field interactions with the dielectric vapor cells to internal surface charges in the vapor cells. The RF fields can scatter off of local environmental features and even reflect within an atom vapor cell[16,17], causing the RF field to be non-uniform over the measurement volume. This non-uniformity generally leads to frequency broadening and additional peaks in the spectrum, which results in a loss of accuracy and signal amplitude. Surface charges are a result of some manufacturing practices and materials and/or are caused by ionization of the atomic vapor inside the cell. While one would like to remove these sources of non-uniformity, this is not always possible. Consequently, understanding their effects on the EIT spectra is important. To this end, we develop a model to understand these effects and investigate some of the more common field non-uniformities experienced in practice. For example, we show results for: (1) a linear gradient in the field across the laser beam propagation path (this type of non-uniformity is present when plate electrodes are used in voltage measurements[18] and other applications[19–21]), (2) an RF standing wave distribution of the E-field (this type of non-uniformity results from vapor cell effects and for some non-ideal applied fields[14,17]), and (3) a step-wise distribution in the RF field across beam propagation path[22], as well as a few others.

We present a model for calculating EIT spectra through spatially-varying electric field amplitudes along the longitudinal beam propagation path by discretizing those changing fields and combining the consequent local transmission values into an aggregate spectrum. This discretization method can generally be applied to any optical parameter; it appears implicitly in many spectral curves and associated with various applications. In this paper, we consider spectral line broadening due to spatial non-uniformity in RF electric field amplitude as measured by the EIT/AT method. Our work suggests that prior works where EIT/AT broadening was observed[7,15–18,23–29] might be reinterpreted in terms of spectral broadening caused by spatially non-uniform E-field amplitude. In fact, the anomalies observed in Ref.[30] are attributed to non-uniform field effects. Here we summarize several characteristic types of distortion and broadening of the EIT signals, each associated with a distinct electric field inhomogeneity. These distorted spectra provide a diagnostic tool that can be used to quantify novel field sources or eliminate experimental imperfections. In particular, rather than losing precision due to EIT lineshape distortions, this technique can yield more information about a particular field's spatial distribution.

In Sec. II, we present the background of typical absorption calculations and our modifications to account for a spatially varying field. In Sec. III, we illustrate the principle with a number of example spectra calculated for various field arrangements using this method. In Sec. IV, we compare the model to measured data observed in different vapor cell arrangements, i.e., a vapor cell embedded in a transmission-line feed and in a vapor embedded in a rectangular waveguide. These comparisons demonstrate the model's ability to characterize field distributions and its accurate prediction of the EIT lineshapes in non-uniform fields. We conclude in Sec. V.

Furthermore, in Sec. A, we describe the master equation underlying the optical calculations.

II. MODELING EIT SIGNALS IN NON-UNIFORM FIELDS

The Rydberg resonant field measurement scheme has been used previously to give traceable measurements of electric field amplitudes[3,9,15]. The corresponding simulation of transmission for a four-level system is well-documented[31,32], and more recently five- and six-level systems[23,33–38] have been developed. Precision measurements using spectroscopy are often limited by the linewidths observed, which can become broadened by non-uniform energy shifts over the observation volume. Here, we focus on the adverse effects on the EIT lineshapes due to variations of the RF electric field amplitude $|E(x)|$ along the laser propagation path, i.e., the x-axis in our case as shown in Fig. 3.

To illustrate the model for both the two-photon ^{133}Cs scheme and the three-photon ^{87}Rb schemes shown in Fig. 1, we first concentrate on the former. The three-photon scheme follows very similarly. In principle, the effect of the E-field non-uniformity of the EIT lineshape would be no different when utilizing either two-photon or three-photon schemes. Nevertheless, we show results (modeling and experiments) for both a two- and three-photon scheme because we have sensors that utilize both types. These two sensors exhibit different types of E-field non-uniformities due to their geometries and, as such, give us two different and independent types of data to compare our model against.

The system we consider is the two-photon scheme shown in Fig. 1(a), where the 'probe' transmission on the D_2 line ($|6S_{1/2}\rangle$ to $|6P_{3/2}\rangle$) through a ^{133}Cs vapor cell is monitored with a photodiode while the detuning Δ_c of a visible 'coupling' laser is scanned across the resonance from the intermediate P state to a highly-excited Rydberg state $|56D_{5/2}\rangle$. In the two-photon scheme, the probe and coupling laser are counter-propagating throughout the vapor cell, see Fig. 3. When a radio frequency signal is resonant ($\Delta_{RF}=0$) with a strong Rydberg-Rydberg transition (in our case $|56D_{5/2}\rangle$ to $|53F_{7/2}\rangle$) with the large dipole moment $\wp_{3,4}$, the Rabi frequency Ω_{RF} gives the frequency-space 'AT splitting' of the new observed line(s)[3,9]:

$$\Omega_{RF}=\frac{\wp_{3,4}|E(x)|}{\hbar}\ , \tag{1}$$

i.e., the line splitting is directly proportional to the applied E-field amplitude.

Using the model presented in Appendix A, we calculate the expected spectrum using Beer's power absorption law of the probe laser with wavelength λ_p, over the extent of the vapor cell length L, where the probe laser transition is given by the imaginary part of the susceptibility χ:

$$T=\frac{P_{out}}{P_{in}}=\exp\left(-\frac{2\pi}{\lambda_p}Im(\chi)L\right). \tag{2}$$

As shown in Appendix A, χ is related to the density matrix component (referred to as the coherence) of the two-photon or three-photon system given in Fig. 1. This density matrix component, ρ_{21}, is obtained from the solution of the master equation. The coherence is a function of the laser detunings and the Rabi frequencies of the optical and RF fields.

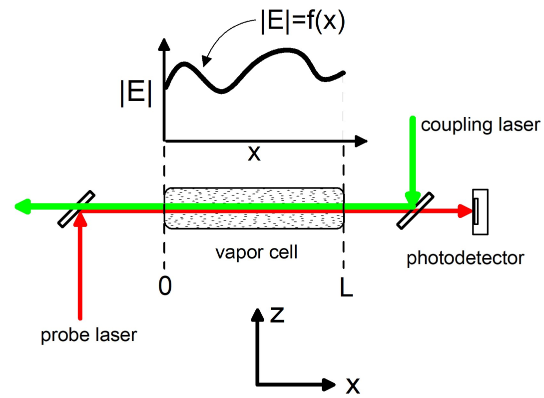

FIG. 3. Diagram of the laser beam propagation direction and the orientation of the E-field amplitude variation inside the vapor cell for all the cases in Fig. 5. The optical field are propagating along the x axis and the E-field amplitude varies along the x axis inside the vapor cell. The optical and RF fields are assumed to be linearly polarized along the y axis.

All of the parameters in this single-medium Beer's law absorption model are assumed fixed over the entire length L. When they vary across the sample region (such as the variability in the applied RF field), further analysis is required to capture the distortion in the EIT lineshape: like the distorted EIT line shown in Fig. 2 for the standing wave case. To model a non-uniform $|E(x)|$ field across the laser beam propagation path, e.g., as depicted in Fig. 3, we use a multi-layer media approach. In this approach, we have discretized space along the laser propagation path (the x-axis) into N_S segments of length $dL=L/N_S$, and we calculated the transmission profile (the EIT signal) for the local $|E(x_i)|$ amplitude over each of them.

We investigate different E-field distributions along the x-axis. An example of the EIT signal for each segment for a linear gradient in the field is shown in Fig. 4. In this example, the optical fields are propagating along the x-axis and the E-field amplitude has a linear variation inside the vapor cell (as would be indicative for the case of non-parallel plate electrodes placed across a vapor cell) along the x-axis as well. These results are for a linearly increasing $|E(x)|$ from 5 to 15 V/m over the laser propagation length of 75 mm, i.e., the length of the vapor cell. Such a linear variation can occur in some situations and could be produced by non-parallel plates when Rydberg sensors are being used for voltage measurements[18] or when parallel-plate electrodes are used in other applications[19–21].

Having generated χ across a scan of Δ_c for many samples of $E(x)$ or $\Omega_{RF}(x)$, one must then combine them into an aggregate spectrum. The transmission through each segment can be calculated using Beer's law with the local susceptibility $\chi(x_i)$ over length dL. To combine transmission spectra, we multiply the sequential transmissions over each of the N_S segments for each value of Δ_c. To simplify multiplying many exponential

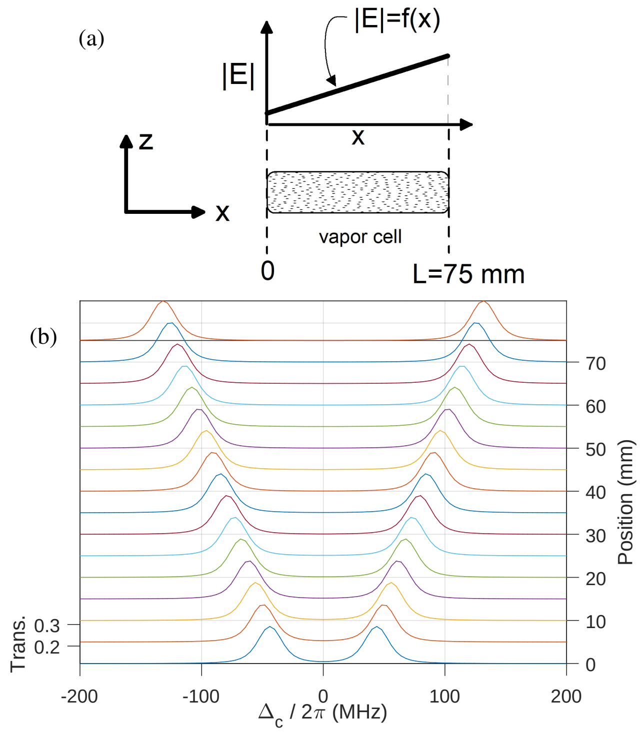

FIG. 4. Example of a linear gradient field and the calculated EIT signal. (a) $E(x)$ is linearly varying from 5 to 15 V/m and sampling occurs every 5 mm of a 75 mm cell. (b) Probe transmission spectra (EIT signal) calculations over space for the linearly varying $E(x)$. The different traces correspond to the EIT signal for different RF field amplitudes inside the vapor cell at the position indicated on the right vertical axis.

functions, we simply sum inside the exponential as:

$$T = \frac{P_{out}}{P_{in}} = \exp\left(-\frac{2\pi L}{\lambda_p N_S}\sum_{i=1}^{N_S} Im\left(\chi\left(x_i\right)\right)\right) \tag{3}$$

where we have taken the constant $dL = L/N_S$ out of the sum. In essence, we 'average' over N_S different susceptibility curves, assuming each sampled field is held constant over L, as plotted in Fig 4(b). In this form, $\chi(x)$ can depend on any number of parameter changes, and gives the total phase delay as well. The EIT signals (i.e., T) obtained from Eq. 3 for different E-field distributions are shown in the next section.

It is important for the sampling density to converge to a smooth physical curve, particularly since sparse sampling leads to large jumps in the peak position from $\Omega_{RF}(x)$ to $\Omega_{RF}(x+dL)$ (i.e., the changes in the E-field strength across the vapor cell) will lead to errors in the calculated resultant curves. The sampling number N_S can be raised to an arbitrary spatial resolution, which is useful for the narrow linewidths typically used in precision experiments.

We note that this broadening gives some additional information about the field non-uniformity experienced by the atoms, i.e., giving many local measurements of the Rabi frequency[39]. These types of measurements might be especially useful as field monitors within other systems, such as our motivating case of low-loss power monitoring within a traditional waveguide. These new peak features can be fit for parameters such as standing wave amplitude, field gradient, etc. by fitting observed lineshapes to ansatz functions. We also note that one potential optimized calculation would be to pre-calculate the spectral curves across a range of $|E|$ values (even interpolating curves). One can then invoke these ansatz functions to combine curves with varying weights rather than calculating an arbitrary function $E(x)$ each time.

III. MODEL RESULTS FOR DIFFERENT FIELD DISTRIBUTIONS

We now provide samples of some common field distributions found in practice and use our simulation method outlined in Sec. II to illustrate the expected probe transmission curves, i.e., the EIT signals. As indicated in Fig. 3, the laser beams are propagating along the x-axis. The E-field amplitude has a prescribed variation along the x-axis inside the vapor cell over its length: $x = 0$ to $x = L$. The modeled results are shown in Fig. 5. Each sub-figure of Fig. 5(a-f) shows the total transmission plot (top left) aggregated over the entire cell length. Its horizontal axis is the coupling detuning Δ_c, and the vertical axis is the probe transmission after propagating across a prescribed E-field amplitude variation inside the vapor cell. The heatmap surface plot (bottom left) gives the transmission spectrum as a function of the detuning (horizontal heatmap axis) and position along the axis of the vapor cell (vertical heatmap axis). The E-field amplitude along the cell is plotted as well (bottom right), where the horizontal axis is the E-field amplitude and the vertical axis specifies the x-axis position it is acquired in the vapor cell. Each field distribution has a maximum of 15 V/m for direct comparison.

The uniform or 'ideal' case is shown in Fig. 5(a). This is synonymous with the single-segment Beer's law approach; it is used as the reference linewidth for the other lineshapes. The step-wise case is shown in Fig. 5(b). This case is physically realized in transverse waveguide probing[22], where atoms are observed in pinholes before and after the central waveguide region in which a constant field is present. We see a large unperturbed peak at the center from the section with no RF field, as well as the expected split AT peaks, with roughly half the height of the center peak (at 1/3 and 2/3 of the total length L).

The linear gradient case is given in Fig. 5(c), with the net transmission spectrum of the model and curves being shown in Fig. 4(b). This linear field gradient case represents a first order modification of the line broadening. It demonstrates that the loss in peak transmission, as well as broadening, characterizes effects from field non-uniformity. For experimental sources, which cause a slight field gradient, the gradient usually grows in proportion to the field amplitude. This effect causes the linewidths to grow with the applied power. This case illustrates, to a first-order approximation of a gradient in the field, that the total FWHM observed is approximately the sum of the total range of $\Omega_{RF}(x)$ induced by $|E(x)|$, plus the non-broadened EIT linewidth.

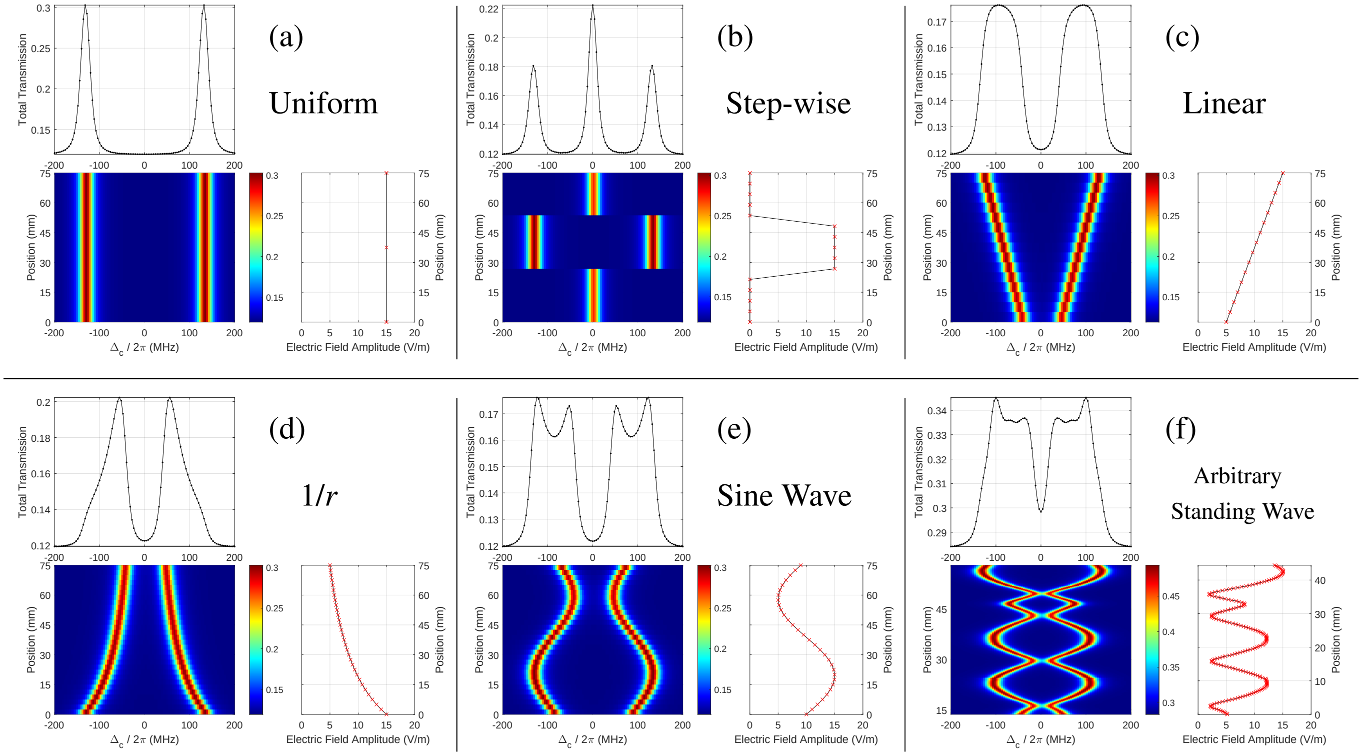

FIG. 5. Simulated total transmission profiles for a variety of cases (a-f) as labelled, and described in Sec. III. For each case, we plot total transmission spectrum (top left), the local transmission spectra over space (bottom left), and the electric field over position (bottom right). While $|E(x)|$ sampling is varied between parts, all simulations use $T = 293$ K, $\Omega_p/2\pi \approx 18$ MHz, $\Omega_c/2\pi \approx 2.6$ MHz, $\Delta_p = \Delta_{RF} = 0$, and $\wp_{3,4}/h \approx 17.5$ MHz/(V/m)

The $1/x$ case is shown in Fig. 5(d). It represents the typical E-field fall-off from a generic antenna, which is typically employed transverse to the sampling path, not along it. Note that the asymmetric peak shape is weighted to the lower end of the field range.

The sine or standing wave case is shown in Fig. 5(e). This field motivated the present investigation. It accounts for the line broadening as the E-field is measured longitudinally within an un-matched waveguide. This EIT signal is similar to that observed in the experimental data shown in Fig. 2. Note the outside 'devil horn' characteristic; it is a result of the sine's sampling density near the extrema.

The case of an arbitrary standing wave pattern is shown in Fig. 5(f). This type of field distribution occurs, for instance, in a retangular waveguide closed with two glass slab ends which cause poor matching between the interior and exterior regions[14,22]. Significantly higher sampling density is required, owing to the spatial gradients involved.

The simulated EIT curves given in Fig. 5 can be used to understand what types of field non-uniformity are present when observing distorted EIT lineshapes in experimental data. In fact, the choices of model parameters used in Fig. 5 are motivated by the experimental observed lineshapes given in Sec. IV.

IV. COMPARISON TO EXPERIMENTAL DATA

In order to validate the application of our theoretical model to experimental results, we show a few different experimental examples compared to EIT lineshapes predicted by it.

A. Twin-lead Waveguide

As the first example, we investigate the effects of longitudinal (along the laser propagation direction) field non-uniformity in a vapor cell placed in a twin-lead waveguide, as depicted in Fig. 6(a). The vapor cell and waveguide are taped to a block of styrofoam in order to hold the device during the experiments. Note that this type of waveguide structure is one method in which a local oscillator field (LO) can be applied to the atoms[11]. This LO approach is a typical method used for the detection of the phase of an incident RF field and has been used for weak field detection via a Rydberg atom-mixer[8,12,13]. The twin-lead wires are attached at each end (defined as port 1 and port 2) to two channels of a single RF source through custom-designed baluns which convert the twin-lead waveguide to an unbalanced 50 ohm impedance. If the excitation of the twin-lead waveguide is imperfect, RF standing waves can develop along the vapor cell which then cause a non-uniform field along the vapor cell. These effects are measured and described in detail next.

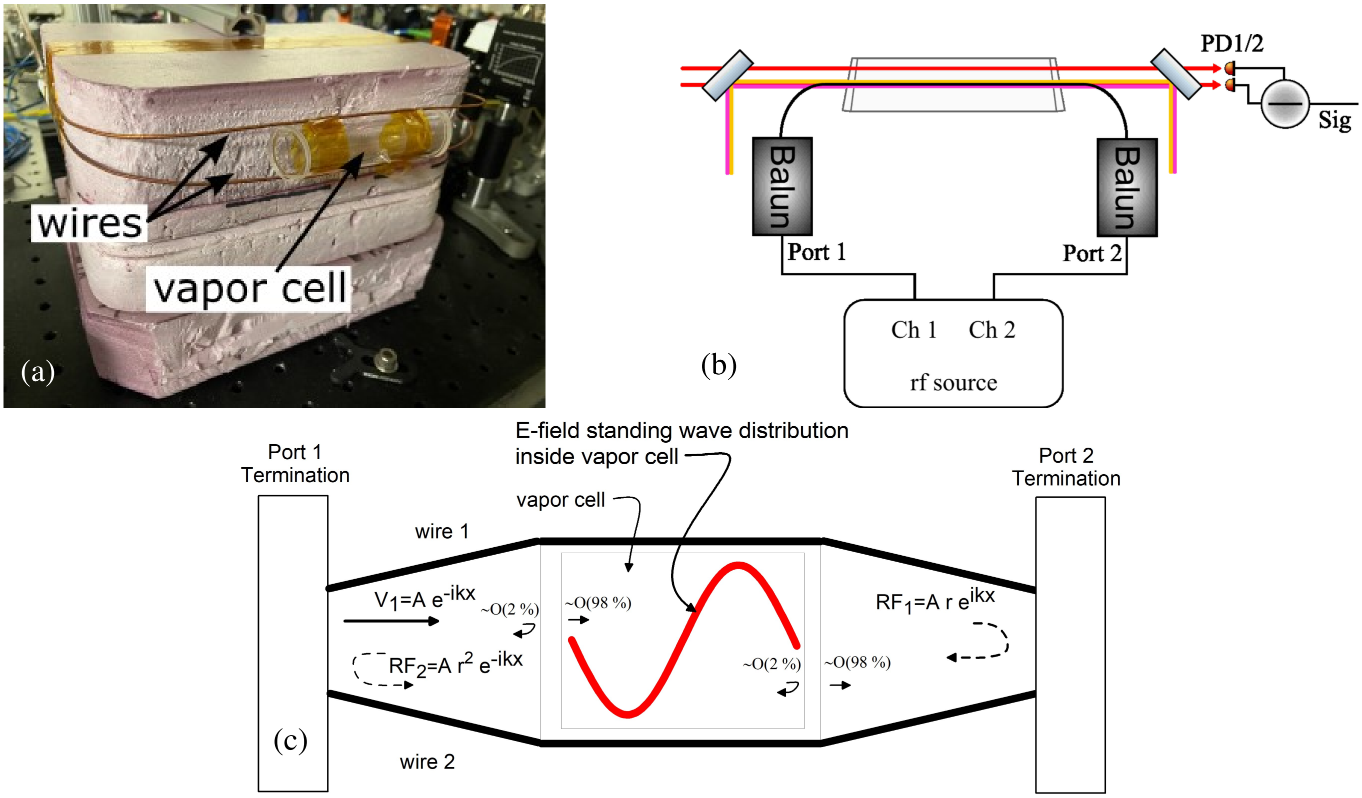

FIG. 6. (a) Vapor cell placed between a twin-lead waveguide. The wires have a diameter of 1.29 mm. The vapor cell is filled with ^{87}Rb, and is 75 mm long, and has an outside diameter of 25 mm. (b) Laser orientation and detection scheme of the three-photon experiments. (c) Reflection along the twin-lead vapor cell structure due to the tapering of the two wires, the vapor cell, the terminations, and the curved wires. Also shown is the E-field standing wave distribution caused by all of the reflections on the twin-line structure.

We use the three-photon scheme shown in Fig. 1(b) to generate EIT in the cell and to demonstrate the RF standing-wave effects on the EIT lineshape. Fig. 6(b) shows the diagram of the measurement setup. It indicates the propagation directions of its three lasers which consist of a 780 nm (probe) laser beam counter-propagating with respect to the 776 nm (dressing) and 1266 nm (coupling) laser beams. We use a differential detection scheme to measure the transmission (the EIT signal) of the probe laser, where the difference measurement [from two photodiodes (PD)] made between the signal 780 nm and a reference separated in the cell as depicted in Fig. 6(b), further details can be found in Ref.[40]. In this experiment, the full-width at half maximum (FWHM) beam diameters for the probe, dressing and coupling lasers, respectively, are 1.38 mm, 1.32 mm, and 1.39 mm. The corresponding powers of the three lasers are 129.95 μW, 12.67 mW, and 214.73 mW. These values correspond to Rabi frequencies of the probe, dress, and coupling lasers of $\Omega_p = 2\pi \cdot 10.02$ MHz, $\Omega_d = 2\pi \cdot 32.52$ MHz, and $\Omega_c = 2\pi \cdot 7.28$ MHz, respectively. In these experiments, the RF E-field and all three optical fields are co-linear polarized, with the E-field vectors pointing from one wire to the other. The schematic in Fig. 6(c) illustrates the interfaces that can give rise to RF reflections that contribute to field inhomogeneities.

As discussed previously, Fig. 2 shows the EIT signal as a function of the coupling laser's detuning (Δ_c) for the case of no RF signal (black curve) on either port of the twin-lead waveguide. The effects of longitudinal field non-uniformity resulting from the RF standing wave on the line can be seen readily by applying an RF signal to ports 1 and 2. We apply $V_1 = A\sin(\omega t)$ and $V_2 = B\sin(\omega t + \phi)$ to ports 1 and 2, respectively, where $\omega = 2\pi \cdot 1.906$ GHz is at the $35F_{7/2} \Longleftrightarrow 35G_{9/2}$ resonant transition in ^{87}Rb.

We begin by considering the RF signal applied only at port 1, with V_1 chosen to produce an E_1 across the vapor cell to be large enough to well-resolve the resulting EIT/AT features. The measured EIT signal for this case is shown in Fig. 7(a) [the blue curve]. We observe cusped features, i.e., two peaks on both EIT lines, and attribute them to longitudinal field non-uniformity in the cell. In fact, upon comparing the shape to the modelled data in Fig. 5(e), we see that a sinusoidal field distribution gives similar EIT lineshapes as those observed experimentally. The sinusoidal field distribution results from a standing wave within the twin-lead waveguide. The standing wave is caused by several factors as illustrated in Fig. 6(c). First, since the vapor cell is made of a dielectric, it will cause reflections of the V_1 signal as it propagates alone the waveguide and interacts with the vapor cell. Secondly, the impedance mismatches due to the termination of the twin-lead at the two ports will also cause reflections. Third, as seen in Fig. 6(a), the twin-leads are not parallel along the propagation path and they are curved around the foam block.

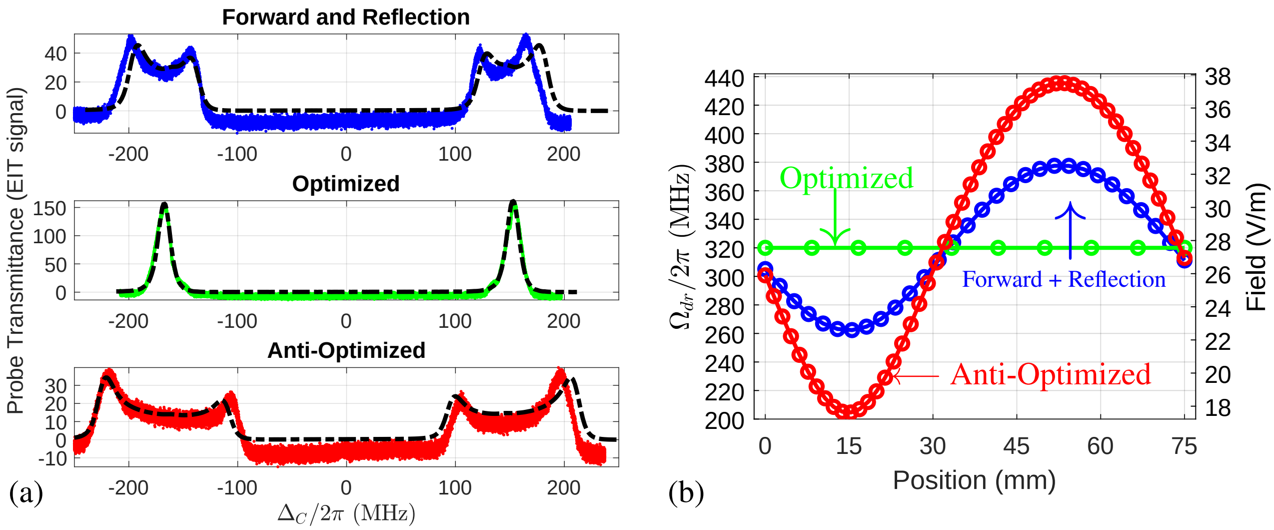

FIG. 7. (a) Experimental (solid traces) and modeled (dashed trace) EIT spectra for different standing waves (graph on left) for the experimental three-photon geometry shown in Fig. 6. (b) Also shown are the spatially-varying E-field amplitude distributions.

This leads to impedance mismatches along the transmission line propagation path and results in additional reflections. All these sources of reflections and impedance mismatches cause a standing-wave voltage waveform and, more importantly, a corresponding E-field (E_1) standing-wave distribution inside the vapor cell (i.e., the magnitude of the E-field seen by the atomic vapor). Furthermore, since the 75 mm vapor cell is near the $\lambda/2$ length for this RF-frequency (79 mm at 1.906 GHz), we attribute an element of these features as arising from the longitudinal non-uniformity due to partial back-reflection(s) inside the vapor cell.

This standing-wave feature can be minimized by injecting a signal into port 2 (i.e., V_2) in order to cancel the reflections of V_1. This idea is similar to using the RF tuner to cancel the reflections in the Rydberg-atom waveguide-power measurements[14], where it is shown that RF tuners can cancel out standing-waves effects and eliminate the EIT lineshape distortion. As such, we find that by applying $V_2 < V_1$ and varying ϕ, we can dramatically modify the lineshape to the extent that the standing wave effects are eliminated. By iteratively tuning V_2 and the inserted phase (ϕ_i) of the RF signal at port 2, we found that we are able to minimize the AT lineshape distortion as illustrated by the solid green trace in Fig 7(a). These optimal values correspond to $V_2 = V_1/5.54$ and $\phi = 290°$. For this case, we see the the EIT/AT peaks are non-distorted and have nearly the Gaussian/Lorentzian lineshapes we expect in a uniform RF field. At this optimized V_2, we found maximal distortion is obtained when a 180° phase shift is added, i.e., when $\phi_i + 180°$. This effect is illustrated with the solid red trace in Fig 7(a). In effect, the added 180° phase induces a larger standing wave of the field by coherently adding to V_1's reflection. These results show that we can constructively or destructively cancel back-reflections by introducing a smaller $V_2(t)$ at port 2, and in effect, cause a non-uniform field to become uniform across the Rydberg sensor.

In order for the model to predict the EIT lineshapes from this experiment, we need to first determine the E-field distribution inside the vapor cell, which can then be the input to the multi-layer model. For the RF signal from port 1, we assume the E-field standing wave inside the vapor cell is approximated by :

$$E_{1model} = C\left[e^{-ikx} + R\,e^{+i(kx+\phi_r)}\right] \quad (4)$$

where $k = 2\pi/\lambda$ and C is the amplitude of the E-field resulting from V_1. The first term in the bracket is the forward traveling wave (propagation in the $+x$ direction). The second term accounts for all the possible reflections which cause the standing wave distribution inside the vapor cell. The parameter R is the magnitude of the reflection coefficient and ϕ_R the reflection's relative phase. We set $R = 0.18$ and $\phi_r = 290°$, i.e., the values of V_2/V_1 and ϕ that gave the optimal lineshape in the above experiments. For the signal from port 2, we assume that it is modeled as

$$E_{2model} = CRe^{+i(kx+\phi_r+\pi)}. \quad (5)$$

When E_{1model} and E_{2model} are added together, a pure traveling wave in the $+x$ direction is obtained, i.e., the standing wave is no longer present.

The E-field distribution inside the vapor obtained from the magnitude of Eqs. (4) and (5) forms a standing wave, shown in Fig. 7(b). These field distributions were used in the model presented in Section II and the resultant EIT/AT signals are shown in Fig. 7(a). Upon comparing the modeled and experimental data, we see that the model predicts the EIT/AT lineshape distortion very well and indicates that the distortion of the measured EIT line is due to the standing wave present in the twin-lead structure.

B. Power Measurements in Rectangular Waveguide

The second example is related to using a Rydberg atom-based sensor to perform SI traceable measurements of RF power in a rectangular waveguide[14,22]. This waveguide used here was designed to allow laser propagation either along the x-axis or the z-axis, see Fig. 8. Details about the measurements described here are given in Ref.[22]. The rectangular waveguide shown in Fig. 8(a) is filled with ^{133}Cs. The first set of data is obtained with the probe and coupling lasers propagating along the x-axis and the E-field is measured along the x-axis inside the waveguide via windows on the top and bottom of the waveguide. This configuration is illustrated in Fig. 8(b). The laser beams are propagating orthogonal to the RF field propagation direction. For this case, the RF E-field is polarized along the x-axis and and both optical fields are polarized along the z-axis. Due to this configuration, we see from Fig. 8(b) that the atoms have a region that is exposed to a nearly constant RF field and two regions that are not exposed to the RF field. Thus, the atoms are exposed to a field distribution similar to the step-function distribution given in Fig. 5(b).

We use the two-photon ^{133}Cs scheme shown in Fig. 1(a) to generate EIT in the waveguide and to measure the RF field distribution effects on the EIT lineshape. A 852 nm (probe) laser beam is counter-propagating with the 511 nm (coupling) laser beam.

In these waveguide experiments, the nominal beam parameters are: FWHM beam diameters for the probe and coupling lasers are 80-120 μm and 400-600 μm, respectively. The powers in the lasers are 20-100 μW and 50-100 mW for probe and coupling, respectively. These values correspond to Rabi frequencies for the probe laser in the few MHz range, and for the coupling laser on the order of 10's of MHz.

Fig. 9 shows the measured EIT/AT signal. Some percentage of the atoms remain unaffected by the field in this case (caused by the zero-field region) and thus exhibit the resonant EIT peak at $\Delta_c = 0$. On the other hand, a portion of the atoms in the field are AT-split as usual. A step-wise field distribution is used with the model in Section II and its predicted results are also given in Fig. 9. A good correlation between the two is observed. There are additional asymmetric effects that distort the spectrum beyond the non-uniformity in the E-field, including spurious EIT peaks resulting from optical reflections off of the viewports, i.e., the optical windows at the end of the vapor cell.

The last example considers a longitudinal standing wave along the z-axis in the waveguide shown in Fig. 8(c). In this case, the RF E-field and both optical fields are co-linear polarized along the x-axis, and the RF and optical fields are propagating along the z-axis. A comparison between experimental and modeled data for this case is shown in Fig. 10. The presence of the inserted glass windows in the waveguide structure holds the atoms and induces a standing wave in the travelling microwave signal. We simulate the field inside of the waveguide using an EM solver for three different power values, each exhibiting varying levels of broadening. We note that a constant offset of ≈ 11 dB between the measured and modeled curves accounts for the significant insertion loss into the waveguide when directional couplers were used in the laboratory. In contrast, the model was fed by an appropriate waveguide mode. Again, we see a good correlation between the experimental and modeled data. Consequently, the distortions in the EIT signals are indeed due to an RF standing wave. Holloway et al.[14] have demonstrated that these distortions of the EIT signals due to the standing wave caused by the end windows can be eliminated, or at least reduced, with RF stub-like tuners.

V. CONCLUSION

We have presented a computational method to approximate the distortions of Rydberg EIT lineshapes due to spatially non-uniform E-field amplitudes inside a vapor cell. We have segmented the optical path, calculated the local transmission values, and then combined these into a composite transmission spectrum. The calculation method is generic and applicable to any alteration in the electric susceptibility parameters when the total transmission or phase delay is monitored. It can therefore help bridge the gap between observed lineshapes and fitting theory curves. We validate our modeling method by demonstrating good agreement between the simulated and experimental atomic spectra in several well defined RF environments. Rather than losing information from broadening, this method enables extracting additional information about the spatial field variations that can be fit to observed transmission spectra. The importance of the simulated EIT curves given in Fig. 5 is that they reveal characteristic lineshape effects based on the type of underlying field inhomogeneity present in the experimental EIT data. Understanding these observed types of distorted EIT lineshapes can facilitate the ability to control and correct effects arising from such nonuniformities. Fig. 5 thus acts as a “Rosetta stone”, translating spatial RF field distributions to EIT/AT atomic spectra. Those results give us a means to understand the effect of different non-uniformities and in turn to achieve fundamental limits on the accuracy and sensitivity for applications such as metrology grade measurements and for atom-based sensors and receivers.

Appendix A: Master-equation model

We use a master-equation model of the EIT signals for the atomic transition schemes used here, shown in Fig. 1. This multi-level EIT model is easily extended from two to three optical photons to examine both of the optical systems considered in this work. The power of the probe beam measured on the detector (the EIT signal, i.e., the probe transmission through the vapor cell) is given by[41]

$$P_{out} = P_{in} \exp\left(-\frac{2\pi L\,\mathrm{Im}[\chi]}{\lambda_p}\right) = P_{in} \exp(-\alpha L) \ , \tag{A1}$$

where P_{in} is the power of the probe beam at the input of the cell, L is the length of the cell, λ_p is the wavelength of the

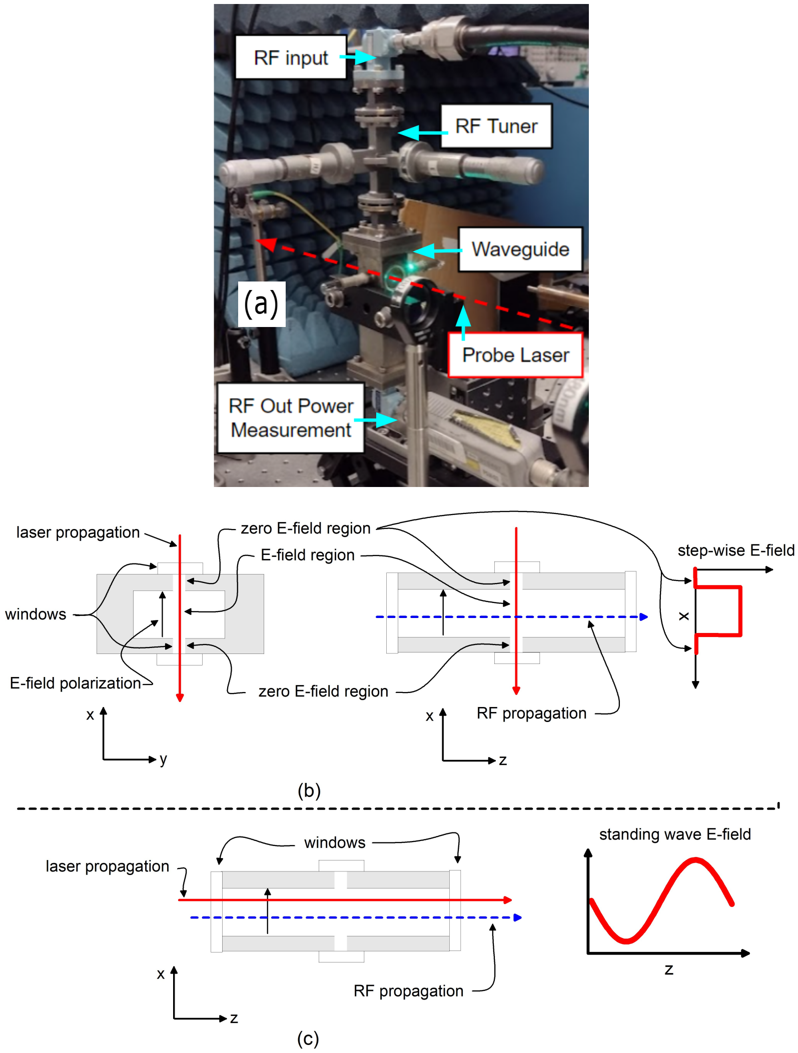

FIG. 8. Rectangular waveguide with laser beams propagating transverse to the RF field propagation: (a) photo of waveguide device, (b) diagram of laser propagation along the x-axis (Also shown are the two regions where the laser beams interact with the atoms in the absence of the RF field.), and (c) diagram of laser propagation along the z-axis. Shown in parts b) and c), are the two different RF field distributions seen by the lasers: step-wise in (a) and standing wave in (b).

probe laser, χ is the susceptibility of the medium seen by the probe laser, and $\alpha = 2\pi \mathrm{Im}[\chi]/\lambda_p$ is Beer's absorption coefficient for the probe laser. The susceptibility for the probe laser is related to the density matrix component (ρ_{21}) by the following expression[31]

$$\chi = \frac{2\mathcal{N}_0 \wp_{12}}{E_p \varepsilon_0} \rho_{21_D} = \frac{2\mathcal{N}_0}{\varepsilon_0 \hbar} \frac{(d\, e\, a_0)^2}{\Omega_p} \rho_{21_D} \ , \tag{A2}$$

where $d = 2.0$ is the normalized transition-dipole moment[42,43] for the probe laser and Ω_p is the Rabi frequency for the probe laser in units of rad/s. The subscript D on ρ_{21} represents a Doppler averaged value. $\mathcal{N}_0$ is the total density of atoms in the cell and is given by

$$\mathcal{N}_0 = \frac{p}{k_B T} \ , \tag{A3}$$

where k_B is the Boltzmann constant, T is temperature in Kelvin, and the pressure p (in units of Pa) is given by[42,43]

$$p = 10^{9.717 - \frac{3999}{T}} \tag{A4}$$

for ^{133}Cs, and

$$p = 10^{9.8630 - \frac{4215}{T}} \tag{A5}$$

for ^{87}Rb.

In eq. (A2), $\wp_{12}$ is the transition-dipole moment for the $|1\rangle$-$|2\rangle$ transition, ε_0 is the vacuum permittivity, and E_p is the amplitude of the probe laser E-field. The density matrix component (ρ_{21}) is obtained from the master equation[31]

$$\dot{\rho} = \frac{\partial \rho}{\partial t} = -\frac{i}{\hbar}[\mathbf{H}, \rho] + \mathscr{L} \ , \tag{A6}$$

where $\mathbf{H}$ is the Hamiltonian of the atomic system under consideration and $\mathscr{L}$ is the Lindblad operator that accounts for the decay processes in the atomic system.

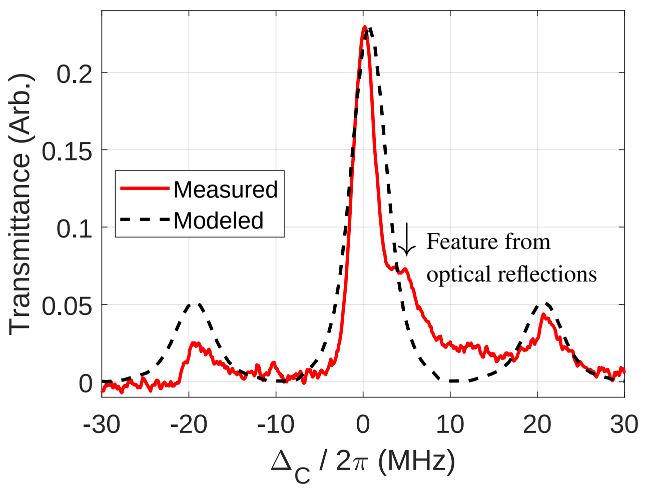

FIG. 9. Comparison of the measured data and corresponding simulated results for a transverse measurement through a waveguide which exhibit a step-wise field behavior. Optical reflections created the additional spectral features in the measured data.

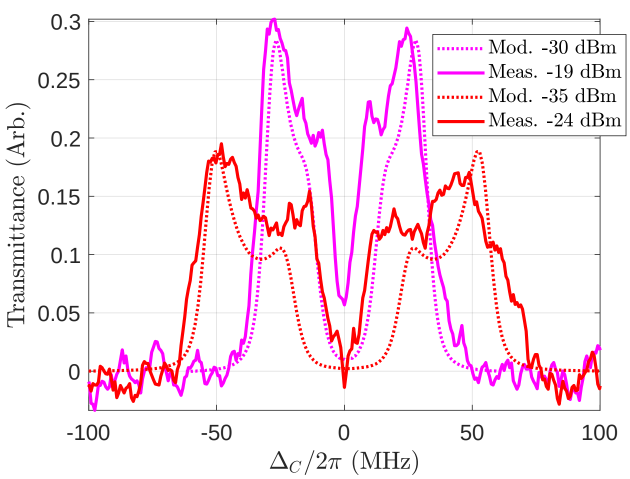

FIG. 10. Comparison of the measured data and corresponding simulated results for a transverse measurement through a waveguide, which exhibit a standing wave behavior. The field distribution in the waveguide was obtained with a commercial electromagnetic field numerical solver.

We numerically solve these equations to find the steady-state solution for ρ_{21} for various values of Rabi frequencies (Ω_i) and detunings (Δ_i). This process is accomplished by forming a matrix with the system of equations for $\dot{\rho}_{ij} = 0$. The null-space of the resulting system matrix is the steady-state solution. The steady-state solution for ρ_{21} is then Doppler averaged[31]:

$$\rho_{21_D} = \frac{1}{\sqrt{\pi}\, u} \int_{-3u}^{3u} \mathscr{R}\, e^{\frac{-v^2}{u^2}}\, dv \ , \quad \text{(A7)}$$

where $u = \sqrt{2k_BT/m}$, m is the mass of the atom. For two-photon ^{133}Cs system

$$\mathscr{R} = \rho_{21}\left(\Delta_p', \Delta_c'\right)$$

and for the three-photon ^{87}Rb system

$$\mathscr{R} = \rho_{21}\left(\Delta_p', \Delta_d', \Delta_c'\right) \ .$$

For the ^{133}Cs system, the probe and coupling beam are counter-propagating and as such the detunings are modified by the following values:

$$\Delta_p' = \Delta_p - \frac{2\pi}{\lambda_p} v \ \text{ and } \ \Delta_c' = \Delta_c + \frac{2\pi}{\lambda_c} v \ . \quad \text{(A8)}$$

For the ^{87}Rb system, the probe beam is counter-propagating to both the dressing and coupling beams and as such, the detunings are modified by the following values:

$$\begin{aligned} \Delta_p' &= \Delta_p - \tfrac{2\pi}{\lambda_p} v \\ \Delta_d' &= \Delta_d + \tfrac{2\pi}{\lambda_d} v \\ \Delta_c' &= \Delta_c + \tfrac{2\pi}{\lambda_c} v \end{aligned} \quad \text{(A9)}$$

We use the technique presented in Ref.[44] to decrease the computational time of the Doppler averaging procedure.

1. Two-Photon Scheme

The two-photon system shown in Fig. 1(a) is a four level system, and the Hamiltonian can be expressed as:

$$H = \frac{\hbar}{2}\begin{bmatrix} 0 & \Omega_p & 0 & 0 \\ \Omega_p & -2\Delta_p & \Omega_c & 0 \\ 0 & \Omega_c & -2(\Delta_p+\Delta_c) & \Omega_{RF} \\ 0 & 0 & \Omega_{RF} & -2(\Delta_p+\Delta_c+\Delta_{RF}) \end{bmatrix} , \quad \text{(A10)}$$

where Δ_p, Δ_c, and Δ_{RF} are the detunings of the probe laser, coupling laser, and the RF source, respectively. The terms Ω_p, Ω_c, and Ω_{RF} are the Rabi frequencies associated, respectively, with the probe laser, coupling laser, and the RF source. The detuning for each fields is defined as

$$\Delta_{p,c,RF} = \omega_{p,c,RF} - \omega_{o_{p,c,RF}} \ , \quad \text{(A11)}$$

where $\omega_{o_{p,c,RF}}$ are the on-resonance angular frequencies of transitions $|1\rangle$-$|2\rangle$, $|2\rangle$-$|3\rangle$, and $|3\rangle$-$|4\rangle$, respectively; and $\omega_{p,c,RF}$ are the angular frequencies of the probe laser, coupling laser, and the RF source, respectively. The Rabi frequencies are defined as $\Omega_{p,c,RF} = |E_{p,c,RF}|\frac{\wp_{p,c,RF}}{\hbar}$, where $|E_{p,c,RF}|$ are the magnitudes of the E-field of the probe laser, the coupling laser, and the RF source, respectively. Finally, $\wp_p$, $\wp_c$ and $\wp_{RF}$ are the atomic dipole moments corresponding to the probe, coupling, and RF transitions.

For the four-level system, the $\mathscr{L}$ matrix is given by

$$\mathscr{L} = \begin{bmatrix} \Gamma_2\rho_{22} & -\gamma_{12}\rho_{12} & -\gamma_{13}\rho_{13} & -\gamma_{14}\rho_{14} \\ -\gamma_{21}\rho_{21} & \Gamma_3\rho_{33}-\Gamma_2\rho_{22} & -\gamma_{23}\rho_{23} & -\gamma_{24}\rho_{24} \\ -\gamma_{31}\rho_{31} & -\gamma_{32}\rho_{32} & \Gamma_4\rho_{44}-\Gamma_3\rho_{33} & -\gamma_{34}\rho_{34} \\ -\gamma_{41}\rho_{41} & -\gamma_{42}\rho_{42} & -\gamma_{43}\rho_{43} & -\Gamma_4\rho_{44} \end{bmatrix} , \quad \text{(A12)}$$

where $\gamma_{ij} = (\Gamma_i + \Gamma_j)/2$ and $\Gamma_{i,j}$ are the transition decay rates. Since the purpose of this study is to explore the non-uniform field limitations of Rydberg-EIT sensing in vapor cells, no collision terms or dephasing terms are added. While decoherence effects are generally present, we have found that the non-uniform field effects are dominant for the cases shown here. Consequently, the collision and dephasing terms were not included in this analysis. While Rydberg-atom collisions, Penning ionization, and ion electric fields can, in principle, cause dephasing, such effects can, for instance, be alleviated by reducing the beam intensities, lowering the vapor pressure, or limiting the atom-field interaction time. In this analysis we set $\Gamma_1 = 0$, $\Gamma_2 = 2\pi\times(4.56\text{ MHz})$, $\Gamma_3 = 2\pi\times(1.3\text{ kHz})$, and $\Gamma_4 = 2\pi\times(2.6\text{ kHz})$. Note that Γ_2 is for the D_2 line in ^{133}Cs[42,45], and Γ_3 and Γ_4 are typical Rydberg decay rates.

2. Three-Photon Scheme

The three-photon system shown in Fig. 1(b) is a five level system, and the Hamiltonian can be expressed as:

$$H = \frac{\hbar}{2}\begin{bmatrix} 0 & \Omega_P & 0 & 0 & 0 \\ \Omega_P & A & \Omega_D & 0 & 0 \\ 0 & \Omega_D & B & \Omega_c & 0 \\ 0 & 0 & \Omega_c & C & \Omega_{RF} \\ 0 & 0 & 0 & \Omega_{RF} & D \end{bmatrix}, \tag{A13}$$

where Ω_P, Ω_D, Ω_c, Ω_{RF} are the Rabi frequencies of the probe laser, dressing laser, coupling laser, and RF field, respectively. Also, the constants

$$\begin{aligned} A &= -2\Delta_P \\ B &= -2(\Delta_P + \Delta_D) \\ C &= -2(\Delta_P + \Delta_D + \Delta_C) \\ D &= -2(\Delta_P + \Delta_D + \Delta_C + \Delta_{RF}), \end{aligned} \tag{A14}$$

where Δ_P, Δ_D, Δ_C, and Δ_{RF} are the detunings of the probe laser, dressing laser, couple laser, and the RF field, respectively, defined as

$$\Delta_{p,d,c,RF} = \omega_{p,d,c,RF} - \omega_{12,23,34,45}, \tag{A15}$$

where $\omega_{12,23,34,45}$ are the on-resonance angular frequencies for the probe, dressing, coupling, and RF fields, respectively.

For the five-level system, the $\mathscr{L}$ matrix is given by:

$$\mathscr{L} = \begin{bmatrix} \Gamma_2\rho_{22} & -\gamma_{12}\rho_{12} & -\gamma_{13}\rho_{13} & -\gamma_{14}\rho_{14} & -\gamma_{15}\rho_{15} \\ -\gamma_{21}\rho_{21} & \Gamma_3\rho_{33} - \Gamma_2\rho_{22} & -\gamma_{23}\rho_{23} & -\gamma_{24}\rho_{24} & -\gamma_{25}\rho_{25} \\ -\gamma_{31}\rho_{31} & -\gamma_{32}\rho_{32} & -\Gamma_3\rho_{33} & -\gamma_{34}\rho_{34} & -\gamma_{35}\rho_{35} \\ -\gamma_{41}\rho_{41} & -\gamma_{42}\rho_{42} & -\gamma_{43}\rho_{43} & \Gamma_3\rho_{33} - \Gamma_4\rho_{44} & -\gamma_{45}\rho_{45} \\ -\gamma_{51}\rho_{51} & -\gamma_{52}\rho_{52} & -\gamma_{53}\rho_{53} & -\gamma_{45}\rho_{45} & -\Gamma_5\rho_{55} \end{bmatrix} \tag{A16}$$

where $\gamma_{ij} = (\Gamma_i + \Gamma_j)/2$ and $\Gamma_{i,j}$ are the transition decay rates. In this analysis we set, $\Gamma_1 = 0$, $\Gamma_2 = 2\pi\times6.065$ MHz, $\Gamma_3 = 2\pi\times1$ MHz, $\Gamma_{4,5} = 2\pi\times(1.3,\ 2.6)$ kHz. Note that Γ_2 is the decay rate for the D2 line in ^{87}Rb, and Γ_4, Γ_5, are typical Rydberg decay rates[43,45].

ACKNOWLEDGMENTS

This work was partially funded by the NIST-on-a-Chip (NOAC) Program and was developed with funding from the Defense Advanced Research Projects Agency (DARPA).The views, opinions and/or findings expressed are those of the authors and should not be interpreted as representing the official views or policies of the Department of Defense or the U.S. Government. A contribution of the US government, this work is not subject to copyright in the United States.

AUTHOR DECLARATIONS

Conflict of Interest

The authors have no conflicts to disclose.

DATA AVAILABILITY STATEMENT

Data is available upon request.

[1] A. Artusio-Glimpse, M. T. Simons, N. Prajapati, and C. L. Holloway, "Modern rf measurements with hot atoms: A technology review of rydberg atom-based radio frequency field sensors," IEEE Microwave Magazine **23**, 44–56 (2022).

[2] J. Gordon, C. Holloway, S. Jefferts, and T. Heavner, "Quantum-based si traceable electric-field probe," 2010 IEEE International Symposium on Electromagnetic Compatibility, July 25-30 , 321–324 (2010).

[3] J. Sedlacek, A. Schwettmann, H. Kubler, R. Low, P. T., and J. Shaffer, "Microwave electrometry with rydberg atoms in a vapour cell using bright atomic resonances," Nature Phys. **8**, 816–824 (2012).

[4] C. Holloway, M. Simons, J. Gordon, P. Wilson, C. Cooke, D. Anderson, and G. Raithel, "Atom-based rf electric field metrology: From self-calibrated measurements to subwavelength and near-field imaging," IEEE Trans. on Electromagnetic Compat. **59**, 717–728 (2017).

[5] M. Tanasittikosol, J. Pritchard, D. Maxwell, A. Gauguet, K. Weatherill, R. Potvliege, and C. Adams, "Microwave dressing of rydberg dark states," J. Phys B **44**, 184020 (2011).

[6] C. L. Holloway, J. A. Gordon, A. Schwarzkopf, D. A. Anderson, S. A. Miller, N. Thaicharoen, and G. Raithel, "Sub-wavelength imaging and field mapping via electromagnetically induced transparency and autler-townes splitting in rydberg atoms," Applied Physics Letters **104**, 244102 (2014).

[7] J. Gordon, C. Holloway, A. Schwarzkopf, D. Anderson, S. Miller, N. Thaicharoen, and G. Raithel, "Millimeter wave detection via autler-townes splitting in rubidium rydberg atoms," Applied Phys. Lett. **105**, 024104 (2014).

[8] J. Gordon, M. Simons, A. Haddab, and C. Holloway, "Weak electric-field detection with sub-1 hz resolution at radio frequencies using a rydberg atom-based mixer," AIP Advances **9**, 045030 (2019).

[9] C. Holloway, J. Gordon, A. Schwarzkopf, D. Anderson, S. Miller, N. Thaicharoen, and G. Raithel, "Broadband rydberg atom-based electric-field probe for si-traceable, self-calibrated measurements," IEEE Trans. on Antenna and Propag. **62**, 6169–6182 (2014).

[10] J. A. Sedlacek, A. Schwettmann, H. Kübler, and J. P. Shaffer, "Atom-based vector microwave electrometry using rubidium rydberg atoms in a vapor cell," Phys. Rev. Lett. **111**, 063001 (2013).

[11] M. Simons, A. Haddab, J. Gordon, D. Novotny, and C. Holloway, "Embedding a rydberg atom-based sensor into an antenna for phase and amplitude detection of radio-frequency fields and modulated signals," IEEE Access **7**, 164975–164985 (2019).

[12] M. Simons, A. Haddab, J. Gordon, and C. Holloway, "A rydberg atom-based mixer: Measuring the phase of a radio frequency wave," Applied Physics Letters **114**, 114101 (2019).

[13] M. Jing, Y. Hu, J. Ma, H. Zhang, L. Zhang, L. Xiao, and S. Jia, "Atomic superheterodyne receiver based on microwave-dressed rydberg spectroscopy," Nature Phys. **16**, 911–915 (2020).

[14] C. Holloway, M. Simons, M. Kautz, A. Haddab, J. Gordon, and C. T.P., "A quantum-based power standard: Using rydberg atoms for a si-traceable radio-frequency power measurement technique in rectangular waveguides," Applied Physics Letters **113**, 094101 (2018).

[15]M. T. Simons, M. D. Kautz, J. A. Gordon, and C. L. Holloway, "Uncertainties in rydberg atom-based rf e-field measurements," in 2018 International Symposium on Electromagnetic Compatibility (EMC EUROPE) (IEEE, 2018) pp. 376–380.
[16]C. Holloway, J. Gordon, A. Schwarzkopf, D. Anderson, S. Miller, N. Thaicharoen, and G. Raithel, "Sub-wavelength imaging and field mapping via electromagnetically induced transparency and autler-townes splitting in rydberg atoms," Applied Phys. Lett. **104**, 244102 (2014).
[17]H. Fan, S. Kumar, J. Sheng, J. P. Shaffer, C. L. Holloway, and J. A. Gordon, "Effect of vapor-cell geometry on rydberg-atom-based measurements of radio-frequency electric fields," Physical Review Applied **4**, 044015 (2015).
[18]C. L. Holloway, N. Prajapati, J. A. Sherman, A. Rüfenacht, A. B. Artusio-Glimpse, M. T. Simons, A. K. Robinson, D. S. La Mantia, and E. B. Norrgard, "Electromagnetically induced transparency based rydberg-atom sensor for traceable voltage measurements," AVS Quantum Science **4**, 034401 (2022).
[19]D. Meyer, P. Kunz, and K. Cox, "Waveguide-coupled rydberg spectrum analyzer from 0 to 20 ghz," Phys. Rev. Applied **15**, 014053 (2021).
[20]B. Liu, L.-H. Zhang, Z.-K. Liu, Z.-Y. Zhang, Z.-H. Zhu, W. Gao, G.-C. Guo, D.-S. Ding, and B.-S. Shi, "Highly sensitive measurement of a megahertz rf electric field with a rydberg-atom sensor," Phys. Rev. Appl. **18**, 014045 (2022).
[21]L. Chai and R. R. Jones, "Demonstration of an rf electrometer based on eit spectroscopy of non-resonantly dressed rydberg atoms," in Conference on Lasers and Electro-Optics (Optica Publishing Group, 2021) p. STu2A.1.
[22]A. Robinson, Microwave Measurements Using Rydberg Atoms, Ph.D. thesis, University of Colorado at Boulder (2022).
[23]A. K. Robinson, A. B. Artusio-Glimpse, M. T. Simons, and C. L. Holloway, "Atomic spectra in a six-level scheme for electromagnetically induced transparency and autler-townes splitting in rydberg atoms," Physical Review A **103**, 023704 (2021).
[24]A. K. Robinson, N. Prajapati, D. Senic, M. T. Simons, and C. L. Holloway, "Determining the angle-of-arrival of a radio-frequency source with a rydberg atom-based sensor," Applied Physics Letters **118**, 114001 (2021).
[25]H. Fan, S. Kumar, R. Daschner, H. Kübler, and J. Shaffer, "Subwavelength microwave electric-field imaging using rydberg atoms inside atomic vapor cells," Optics Letters **39**, 3030–3033 (2014).
[26]D. T. Stack, P. D. Kunz, D. H. Meyer, and N. Solmeyer, "Microwave electric field sensing with rydberg atoms," in Quantum Information and Computation IX, Vol. 9873 (International Society for Optics and Photonics, 2016) p. 987306.
[27]D. A. Anderson, S. A. Miller, G. Raithel, J. Gordon, M. Butler, and C. Holloway, "Optical measurements of strong microwave fields with rydberg atoms in a vapor cell," Physical Review Applied **5**, 034003 (2016).
[28]A. Chopinaud and J. D. Pritchard, "Optimal state choice for rydberg-atom microwave sensors," Physical Review Applied **16**, 024008 (2021).
[29]M. T. Simons, J. A. Gordon, and C. L. Holloway, "Fiber-coupled vapor cell for a portable rydberg atom-based radio frequency electric field sensor," Applied Optics **57**, 6456–6460 (2018).
[30]M. G. Bason, M. Tanasittikosol, A. Sargsyan, A. Mohapatra, D. Sarkisyan, R. Potvliege, and C. Adams, "Enhanced electric field sensitivity of rf-dressed rydberg dark states," New Journal of Physics **12**, 065015 (2010).
[31]P. R. Berman and V. S. Malinovsky, Principles of Laser Spectroscopy and Quantum Optics (Princeton University Press, Princeton, 2011).
[32]C. Holloway, M. Simons, J. Gordon, A. Dienstfrey, D. Anderson, and G. Raithel, "Electric field metrology for si traceability: Systematic measurement uncertainties in electromagnetically induced transparency in atomic vapor," J. of Applied Physics **121**, 233106 (2017).
[33]N. Thaicharoen, K. R. Moore, D. A. Anderson, R. C. Powel, E. Peterson, and G. Raithel, "Electromagnetically induced transparency, absorption, and microwave-field sensing in a rb vapor cell with a three-color all-infrared laser system," Phys. Rev. A **100**, 063427 (2019).
[34]J. P. Shaffer and H. Kübler, "A read-out enhancement for microwave electric field sensing with Rydberg atoms," in Quantum Technologies 2018, Vol. 10674, edited by J. Stuhler, A. J. Shields, and M. J. Padgett, International Society for Optics and Photonics (SPIE, 2018) p. 106740C.
[35]C. Carr, M. Tanasittikosol, A. Sargsyan, D. Sarkisyan, C. S. Adams, and K. J. Weatherill, "Three-photon electromagnetically induced transparency using rydberg states," Opt. Lett. **37**, 3858–3860 (2012).
[36]N. Prajapati, N. Bhusal, A. P. Rotunno, S. Berweger, M. T. Simons, A. B. Artusio-Glimpse, Y. J. Wang, E. Bottomley, H. Fan, and C. L. Holloway, "Sensitivity comparison of two-photon vs three-photon rydberg electrometry," (2022), arXiv:2211.11848 [physics.atom-ph].
[37]M. Simons, A. Artusio-Glimpse, C. Holloway, E. Imhof, S. Jefferts, R. Wyllie, B. Sawyer, and T. Walker, "Continuous radio frequency electric-field detection through adjacent rydberg resonance tuning," Phys. Rev. A (2021).
[38]S. Berweger, N. Prajapati, A. B. Artusio-Glimpse, A. P. Rotunno, R. Brown, C. L. Holloway, M. T. Simons, E. Imhof, S. R. Jefferts, B. N. Kayim, M. A. Viray, R. Wyllie, B. C. Sawyer, and T. G. Walker, "Rydberg state engineering: A comparison of tuning schemes for continuous frequency sensing," (2022), arXiv:2209.14407 [physics.atom-ph].
[39]M. Sahrai, M. Mahmoudi, and R. Kheradmand, "Atom localization of a two-level pump-probe system via the absorption spectrum," Laser physics **17**, 40–44 (2007).
[40]R. C. Brown, B. Kayim, M. A. Viray, A. R. Perry, B. C. Sawyer, and R. Wyllie, "Very-high- and ultrahigh-frequency electric-field detection using high angular momentum rydberg states," Phys. Rev. A **107**, 052605 (2023).
[41]A. Yarin, Optical Electronics, 4th ed. (CBS College Publishing, New York, 1995).
[42]D. A. Steck, "Cesium D line data," http://steck.us/alkalidata (1998), revision 2.2.1, 21 November 2019.
[43]D. Steck, "Rubidium 87 d line data," available online at http://steck.us/alkalidata (revision 2.1.6, 20 September 2013) (2001).
[44]A. P. Rotunno, A. K. Robinson, N. Prajapati, S. Berweger, M. T. Simons, A. B. Artusio-Glimpse, and C. L. Holloway, "Inverse transform sampling for efficient doppler-averaged spectroscopy simulations," AIP Advances **13**, 075218 (2023).
[45]N. Šibalić, J. D. Pritchard, C. S. Adams, and K. J. Weatherill, "Arc: An open-source library for calculating properties of alkali rydberg atoms," Comput. Phys. Commun. **220**, 319–331 (2017).